

Submitted for publication in *The Astrophysical Journal*

New Light in Star-Forming Dwarf Galaxies: The PMAS Integral Field View of the Blue Compact Dwarf Galaxy Mrk 409¹

Luz M. Cairós

luzma@aip.de

Astrophysikalisches Institut Potsdam, An der Sternwarte 16, D-14482 Potsdam, Germany

Nicola Caon

nicola.caon@iac.es

*Instituto de Astrofísica de Canarias, E-38200 La Laguna, Tenerife, Spain and
Departamento de Astrofísica, Universidad de la Laguna, E-38205, La Laguna, Tenerife,
Spain*

Polychronis Papaderos

papaderos@astro.up.pt

*Centro de Astrofísica da Universidade do Porto, Rua das Estrelas, 4150-762 Porto,
Portugal and Instituto de Astrofísica de Andalucía (CSIC), C/ Camino Bajo de Huétor 50,
18008 Granada, Spain*

Carolina Kehrig

kehrig@aip.de

Astrophysikalisches Institut Potsdam, An der Sternwarte 16, D-14482 Potsdam, Germany

Peter Weilbacher

pweilbacher@aip.de

Astrophysikalisches Institut Potsdam, An der Sternwarte 16, D-14482 Potsdam, Germany

Martin M. Roth

mmroth@aip.de

Astrophysikalisches Institut Potsdam, An der Sternwarte 16, D-14482 Potsdam, Germany

Cristina Zurita

czurita@iac.es

*Instituto de Astrofísica de Canarias, E-38200 La Laguna, Tenerife, Spain and
Departamento de Astrofísica, Universidad de la Laguna, E-38205, La Laguna, Tenerife,
Spain*

ABSTRACT

We present an integral field spectroscopic study of the central 2×2 kpc² of the blue compact dwarf galaxy Mrk 409, observed with the *Potsdam MultiAperture Spectrophotometer*. This study focuses on the morphology, two-dimensional chemical abundance pattern, excitation properties and kinematics of the ionized interstellar medium in the starburst component. We also investigate the nature of the extended ring of ionized gas emission surrounding the bright nuclear starburst region of Mrk 409. PMAS spectra of selected regions along the ring, interpreted with evolutionary and population synthesis models, indicate that their ionized emission is mainly due to a young stellar population with a total mass of $\sim 1.5 \times 10^6 M_{\odot}$, which started forming almost coevally ~ 10 Myr ago. This stellar component is likely confined to the collisional interface of a spherically expanding, starburst-driven super-bubble with denser, swept-up ambient gas, ~ 600 pc away from the central starburst nucleus. The spectroscopic properties of the latter imply a large extinction ($C_{H\beta} > 0.9$), and the presence of an additional non-thermal ionization source, most likely a low-luminosity Active Galactic Nucleus. Mrk 409 shows a relatively large oxygen abundance ($12 + \log(\text{O}/\text{H}) \sim 8.4$) and no chemical abundance gradients out to $R \sim 600$ pc. The ionized gas kinematics displays an overall regular rotation on a northwest-southwest axis, with a maximum velocity of 60 km s^{-1} ; the total mass inside the star-forming ring is about $1.4 \times 10^9 M_{\odot}$.

Subject headings: galaxies: dwarf galaxies - galaxies: starburst - galaxies: compact - galaxies: stellar populations - galaxies: individual (Mrk 409)

¹Based on observations obtained at the German-Spanish Astronomical Center, Calar Alto, operated by the Max-Planck-Institut für Astronomie Heidelberg jointly with the Spanish National Commission for Astronomy.

1. Introduction

Blue Compact Dwarf (BCD) galaxies are systems undergoing violent bursts of star formation (Sargent & Searle 1970), that appear compact in the optical (starburst diameter ≤ 1 kpc), and have low intrinsic luminosities ($M_B \geq -18$ mag) and low gas-phase metallicities ($7.1 \leq 12 + \log(\text{O}/\text{H}) \lesssim 8.3$). These characteristics make them excellent nearby laboratories for investigating some of the most outstanding questions in the contemporary extragalactic astronomy: i) they are suitable sites to study the process of galaxy formation and evolution, as they are thought to be the local analogs of the building blocks from which larger systems were formed at high redshift (Kauffmann et al. 1993); ii) they allow the determination of the primordial helium abundance with a minimum of extrapolation to early conditions (Pagel et al. 1992; Izotov et al. 2007); and, iii) being smaller and less massive than normal galaxies, BCDs neither can sustain spiral density waves, nor suffer from disk instabilities, hence they permit the investigation of the star-formation process in a relatively simple environment.

In order to properly characterize the BCD galaxy class, and to get insights into the above topics, detailed spectrophotometric analysis of individual objects, aimed to disentangle their different stellar populations and to elucidate their star-forming histories (SFH), are imperative (see, e.g., Cairós et al. 2002, 2007). However, very few such studies have been done so far (Papaderos et al. 2002, 2006; Noeske et al. 2000; Gil de Paz et al. 2000; Fricke et al. 2001; Guseva et al. 2001; Cairós et al. 2002, 2007). These works, all based on traditional observing techniques (broad- and narrow-band imaging plus long-slit spectroscopy), have shown that combining spectroscopy and surface photometry is indeed essential for tackling the problem of BCD evolution. However, they suffer from several drawbacks, the most severe being the large amount of observing time that they require: acquiring images in several broad- and narrow-band filters, in addition to a series of long-slit exposures sweeping the region of interest, translate into prohibitively long observing times of two or more nights per galaxy. This usually means that the data are taken under varying atmospheric conditions and, potentially, slight differences in the instrumental setup. Clearly, uncertainties in the combination of such a data set will propagate throughout in the data analysis and interpretation. Long-slit spectroscopy has also the additional problem of the uncertainty on the exact location of the slit.

The relatively new observational method of Integral Field Spectroscopy (IFS) overcomes these problems. Detailed IFS studies have been carried out for SBS 0335-052 E with VLT/GIRAFFE (Izotov et al. 2006), for the low-luminosity BCD II Zw 70 with CAHA 3.5m/PMAS (Kehrig et al. 2008), for five luminous BCDs with WHT/INTEGRAL (García-Lorenzo et al. 2008), for UM 408 with GMOS-IFU (Lagos et al. 2009) and for Mrk 1418 with PMAS

(Cairós et al. 2009). Although the scope of these studies is somehow limited by a small field of view (FOV) or by low spectral resolution, they convincingly demonstrate that IFS is the method of choice for small, yet complex star-forming (SF) objects like BCDs. Each single exposure of an integral field spectrograph provides both spatial and spectral information, making the observations an order of magnitude more efficient than any traditional observing technique. Furthermore, IFS provides simultaneously spectra for all spatial resolution elements, under the same instrumental and atmospheric conditions, which guarantees the homogeneity of the dataset.

Systems with a high degree of asymmetry in their SF component, such as BCDs, hosting two or more well-separated SF regions, can be studied in a comprehensive manner only with 2D spectroscopy. Long standing questions in the field, as the propagation of the star-formation, the generation and dispersal of heavy elements or the abundance gradients, can be approached efficiently only with IFS instruments.

While existing works indicate that the SF activity in BCDs proceeds largely in bursts (e.g., Krüger & Fritze-v. Alvensleben 1994; Mas-Hesse & Kunth 1999), we are still lacking an understanding of the two-dimensional star-formation pattern. Established is solely that, in the majority (90%) of BCDs, the SF regions are not randomly scattered within the low surface brightness (LSB) host, but rather confined to its central part, out to ~ 2 exponential scale lengths (Papaderos et al. 1996; Cairós et al. 2001). This fact suggests a physical link between the mode of the SF activity in BCDs and the shape of the gravitational potential formed by the old, higher mass-to-light (M/L) ratio stellar LSB host.

Some of the most metal-poor BCDs, thought to be still in the process of their formation, such as SBS 0335-052 E (Thuan et al. 1997; Papaderos et al. 1998) or SBS 1415+437 (Thuan et al. 1999; Guseva et al. 2003; see Papaderos et al. 2008 for a review), present clear signatures of uni-directional SF propagation. This process can lead to a *cometary* morphology, with the “comets head” (the dominant SF region) located at the tip of an elongated LSB host delineating the trail of past propagating SF activities (Papaderos et al. 2008). An irregular SF propagation pattern in form of a random-walk was reported by a detailed analysis of individual stellar clusters in the luminous BCD ESO 338-IG04 (Östlin et al. 2003), while the potential role of SF propagation in Mrk 370 and Mrk 35 has been discussed in Cairós et al. (2002) and Cairós et al. (2007), respectively.

In the two BCDs Mrk 86 and Mrk 409, the ring-morphology of the SF regions suggests that the SF activity could have been triggered by the shock wave produced by multiple SNe in a central starburst. In the case of Mrk 86, extensive studies (Gil de Paz et al. 2000, 2002) support this hypothesis. However, because of the small spatial and spectral coverage of the available spectroscopic observations (Gil de Paz et al. 2003a, hereafter GdP03), conclusive

results for Mrk 409 can not be drawn.

In this paper we show the great potential of IFS when applied to BCDs by presenting a pilot study focused on the galaxy Mrk 409 (= NGC 3011). Mrk 409 is a luminous ($M_B = -17.73$) BCD, belonging to the nE morphological class (Loose & Thuan 1986). Its intriguing gas ionized morphology — a compact nuclear starburst region surrounded by two SF rings at projected galactocentric radii of $5''$ and $18''$, corresponding to 0.64 and 2.3 kpc — makes it an excellent laboratory for investigating the star-formation pattern and abundance gradients in BCDs. We observed the galaxy with the PMAS spectrograph mounted on the 3.5m Calar Alto telescope. The PMAS field of view ($2 \times 2 \text{ kpc}^2$ at the Mrk 409 distance) allows us to map the nuclear region and the inner SF ring. The basic parameters of the galaxy are summarized in Table 1.

The paper is organized as follows: in Sect. 2 we describe the observations, the data analysis and the method employed to derive the two dimensional maps. In Sect. 3 we present continuum and emission line intensity, line ratio and velocity maps as well as results from the analysis of the integrated spectra of the SF regions identified in the galaxy. The results are discussed and summarized in Sect. 4 and Sect. 5, respectively.

2. The Data

2.1. Observations and Data Reduction

Mrk 409 was observed in 2007 March, with the *Potsdam MultiAperture Spectrophotometer* (PMAS) attached to the 3.5m telescope of the Observatorio Astronómico Hispano Alemán Calar Alto (CAHA). PMAS is an integral field spectrograph, with a lens array of $16'' \times 16''$ ($2 \times 2 \text{ kpc}^2$ at the Mrk 409 distance) square elements. This array is connected to a bundle of fiber optics, whose 256 fibers are re-arranged to form a pseudo-slit in the focal plane of the fiber spectrograph. In the configuration used each fiber corresponds to a spatial sampling on the sky of $1'' \times 1''$ (see Roth et al. 2005; Kelz et al. 2006 for more details about the instrument). A grating with 300 grooves per mm was used during the observations, in combination with a 2048×4096 pixel SITe ST002A CCD detector; this provides a spectral range of 3590–6996 Å with a linear dispersion of 3.2 Å per pix and a resolution (FWHM) of about 7 Å.

We observed a total of 6000 sec on the galaxy, with the integration time split into five exposures of 1200 sec each; additional sky frames were taken moving the telescope several arcmin away from the target position. Calibration frames were observed before and after the galaxy exposures. These calibrations consist of spectra of emission line lamps (HgNe lamp),

Table 1. Basic data for Mrk 409

Parameter	Data	Note
Other names	NGC 3011, UGC 5259	
RA (2000)	09 49 41	
DEC (2000)	+32 13 16	
v_{helio} (km s ⁻¹)	1527	
D (Mpc)	26.3	
A_B (mag)	0.071	(1)
M_B (mag)	-17.73	
m_B (mag)	14.37 ± 0.03	(2)
m_R (mag)	13.33 ± 0.05	(2)
$F(\text{H}\alpha)$ (ergs s ⁻¹ cm ⁻²)	$2.93 \pm 0.17 \times 10^{-13}$	(2)
m_J (mag)	11.88 ± 0.02	(3)
m_H (mag)	11.34 ± 0.03	(3)
m_{K_s} (mag)	11.17 ± 0.04	(3)
M_{HI} (M_{\odot})	0.31×10^9	(4)
M_{T} (M_{\odot})	0.33×10^{10}	(4)

Note. — Coordinates, heliocentric velocity and distance, all taken from NED (<http://nedwww.ipac.caltech.edu/>). Distance calculated using a Hubble constant of 73 km s⁻¹ Mpc⁻¹, and taking into account the influence of the Virgo Cluster, the Great Attractor and the Shapley supercluster. Absolute magnitude in the B band, computed from the tabulated integrated B magnitude and distance. (1) Absorption coefficient in the B band, from Schlegel et al. (1998). (2) Gil de Paz et al. (2003b). (3) From 2MASS. (4) Neutral hydrogen mass M_{HI} and total mass M_{T} from Thuan & Martin (1981).

which are required to perform the wavelength calibration, and spectra of a continuum lamp, necessary to locate the fiber spectra on the CCD and to perform the flat-fielding correction. The spectrophotometric standard stars BD+75325 and BD+332642 were observed for flux calibration. As usual, bias and sky-flat exposures were taken at the beginning and at the end of the night. The seeing was about 1.8 arcsec.

The data were processed using standard IRAF² tasks. The reduction procedure included bias subtraction and image trimming, tracing and extraction, wavelength and distortion calibration, flat-fielding, combination of the individual frames, sky subtraction and flux calibration. For a detailed description of the individual steps performed in fiber data processing see Cairós et al. (2009). The typical errors on the wavelength calibration are 0.02 Å. The flux calibration was carried out using our observations of spectrophotometric standard stars. By comparing the sensitivity curves obtained for all the spectrophotometric standards observed throughout the three nights of the observing run, we estimate that the relative uncertainty on the calibration factor is generally equal or less than 2%, except blueward of 4000 Å, where the curves show a marked change of slope and the uncertainty increases up to about 8%.

2.2. Line Fitting and Map Generation

In this study we generate 2D intensity maps for the most important emission lines as well as for different continuum regions. The relevant parameters of the emission lines (center, flux and equivalent width) were determined by fitting single Gaussians; the fit was carried out by using the χ^2 minimization algorithm implemented by C. B. Markwardt in the *mpfitexpr* IDL library (Markwardt 2009). The H β line, in which the absorption component was also visible, was modeled as the sum of two Gaussians. The continuum (typically 30–50 Å on both sides) was fitted by a straight line. Lines in a doublet were fitted imposing that they have the same redshift and width.

Criteria such as flux, error on flux, velocity and width were used to do a first, automatic assessment of whether to accept or reject a fit. For instance, lines with too small (less than the instrumental width) or too large (> 5 Å) widths were flagged out, similar to lines with an error on the flux of more than about 10% (the exact limits depending on the specific line). In order to improve the reliability and stability of fits invoking both an absorption and emission component, an additional criterion was applied to the equivalent width of the

²IRAF is distributed by the National Optical Astronomy Observatories, which are operated by the Association of Universities for Research in Astronomy, Inc., under cooperative agreement with the National Science Foundation.

absorption component (allowed to vary between 0 and 5 Å).

Each individual fit was visually checked, and when necessary, the aforementioned automated quality criteria were overridden (see Cairós et al. 2009).

The fit procedure gives, for each spectral line, a table with the spaxel number and the values of the measured parameter; this table is then used to build a 2D spatial map. Continuum maps were built in the same way by summing the signal within wavelength intervals free from emission lines or strong sky-lines residuals.

3. Results

3.1. Continuum and Emission Line Intensity Maps

The main advantage of IFS is that it maps an object simultaneously in different continuum bands and emission lines, so that we can obtain at the same time the spatial distribution of the stellar component and of the ionized gas emission. We constructed continuum and flux maps of the brightest emission lines in Mrk 409. To allow a quick comparison with our results, the *B*-band and H α images of the galaxy (Gil de Paz et al. 2003b) are displayed in Figure 1.

Figure 2 displays the [O II] λ 3727, H β , [O III] λ 5007, [O I] λ 6300, H α , [N II] λ 6584 and [S II] λ 6717, 6731 emission-line maps. These maps trace the regions of recent star formation. In all maps except one Mrk 409 shows a similar, irregular pattern, with a number of SF knots distributed in a ring of diameter \simeq 5 arcsec (600 pc) around the nuclear starburst (region #3); the ring is resolved into at least five smaller SF knots. Only in [O I] λ 6300 the galaxy has a strikingly different morphology, revealing solely a single prominent central peak. The presence of strong [O I] λ 6300 is an indicator that power-law photoionization or shock-heating are important in the nuclear region of Mrk 409.

The stellar continuum emission in the spectral range 4500–4700 Å is also shown in Figure 2. This map displays a regular morphology with elliptical isophotes with nearly constant position angle, and a well defined central peak, whose location is the same in all continuum bands and also coincides with the nuclear SF region #3.

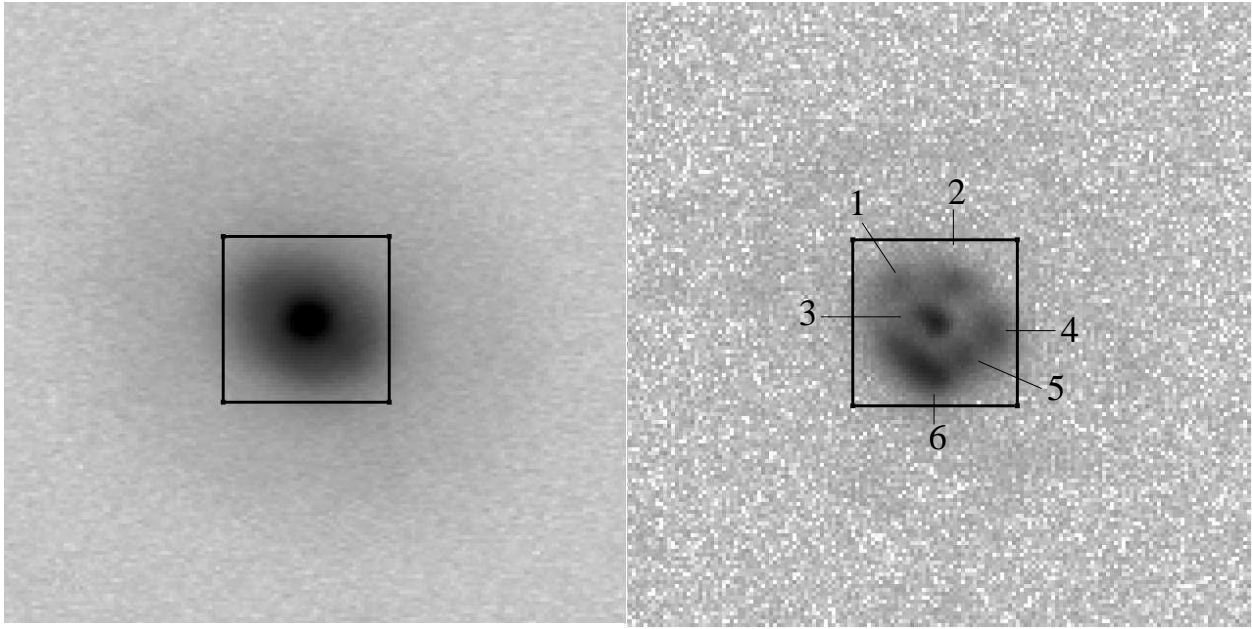


Fig. 1.— *left panel*: B-band image of Mrk 409; the central box indicates the field of view covered by our PMAS observations; *right panel*: Continuum-subtracted $H\alpha$ image with the individual SF knots labeled. The field of view is one arcmin in both frames. North is up, east to the left. Both images, retrieved from the NED, are published in Gil de Paz et al. (2003b)

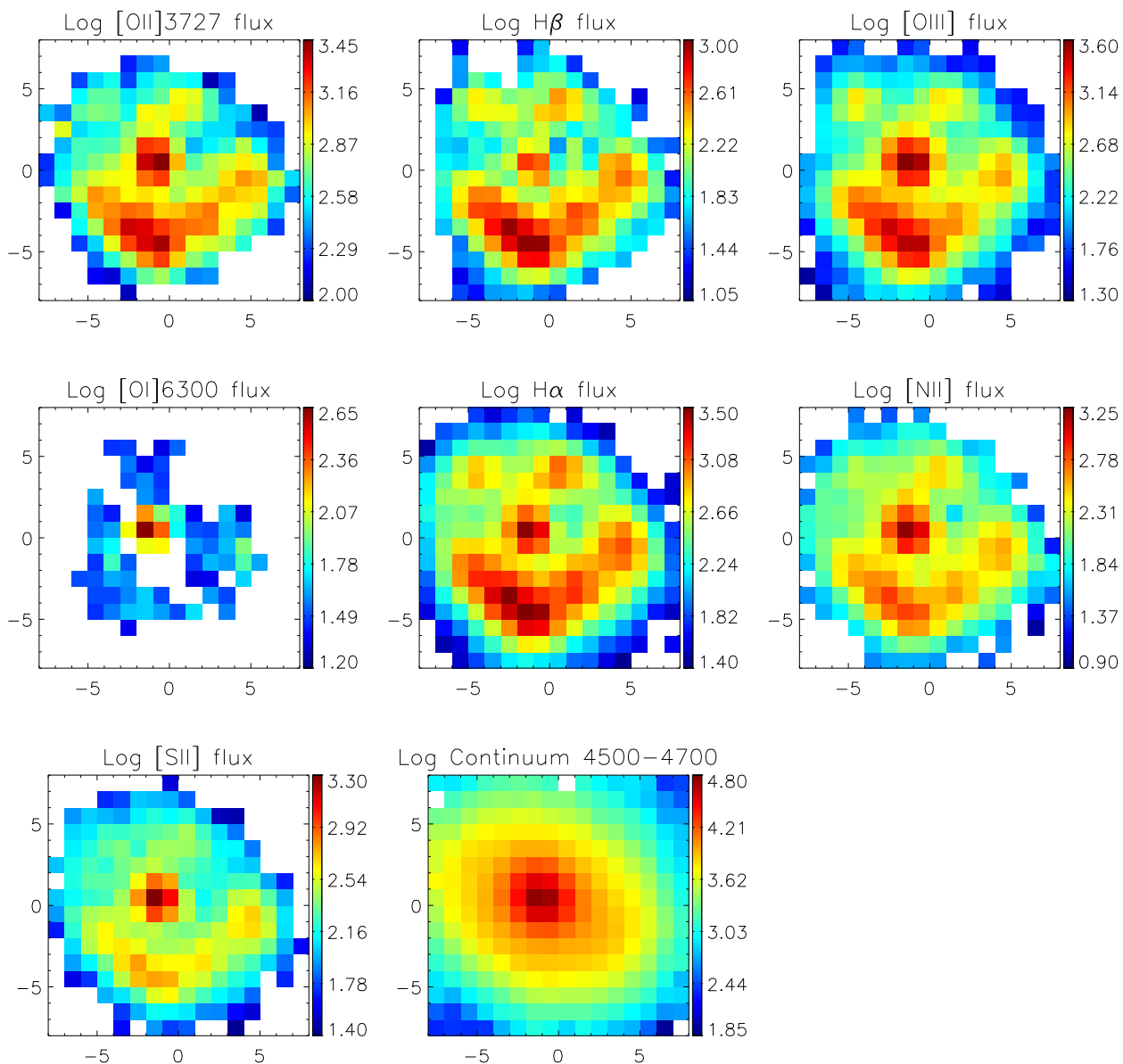


Fig. 2.— Emission line intensity maps derived from Gaussian fits to each line and spaxel (see text for details): [O II] λ 3727; H β ; [O III] λ 5007; [O I] λ 6300; H α ; [O III] λ 5007; [S II] λ 6717, 6731. The last panel shows the continuum emission between 4500 and 4700 \AA , a spectral region free from line emission (“pure continuum”). North is up, east to the left. Axis units are arcseconds. All images are shown in logarithmic scale to bring up the fainter regions. Flux units are $10^{-18} \text{ erg cm}^{-2} \text{ s}^{-1} \text{ \AA}^{-1}$.

3.2. Line Ratio Maps

In order to investigate the main ionization mechanisms operating in Mrk 409, we built the [O III] $\lambda 5007/\text{H}\beta$, [O I] $\lambda 6300/\text{H}\alpha$, [N II] $\lambda 6584/\text{H}\alpha$ and [S II] $\lambda\lambda 6717, 6731/\text{H}\alpha$ line ratio maps, shown in Figure 3. In these maps high excitation corresponds to high values of [O III] $\lambda 5007/\text{H}\beta$, and to low values of [N II] $\lambda 6584/\text{H}\alpha$ and [S II] $\lambda\lambda 6717, 6731/\text{H}\alpha$. All the excitation maps display a similar pattern. In the SF knots in the ring, the values of the different ratios are those characteristic of H II regions. In the central starburst, however, opposite to what is expected in regions photoionized by stars, high values for all ratios are found: [O III] $\lambda 5007/\text{H}\beta \geq 6$; [O I] $\lambda 6300/\text{H}\alpha > 0.2$; [N II] $\lambda 6584/\text{H}\alpha > 0.5$; [S II] $\lambda\lambda 6717, 6731/\text{H}\alpha > 1$), most probably indicating the presence of an additional ionization mechanism — an *Active Galactic Nucleus* (AGN) or shocks.

The extinction in the galaxy (Figure 3) has been derived from the $\text{H}\alpha/\text{H}\beta$ ratio. Mrk 409 displays an inhomogeneous extinction pattern, which peaks in the nuclear starburst. In this region the $\text{H}\alpha/\text{H}\beta$ line ratio rises to values as high as 6, suggesting strong extinction by dust with a reddening $E(B - V)$ of up to $\simeq 0.70$ mag. By contrast, in the circumnuclear SF knots the $\text{H}\alpha/\text{H}\beta$ ratio is only slightly larger than the nominal value of 2.86 (Osterbrock & Ferland 2006), and implies $E(B - V) \lesssim 0.2$. Note that, applying the extinction derived in the central region to the whole SF component, as is usually done in long-slit or single-aperture spectroscopic studies (with, e.g., the SDSS), would lead to a large overestimate of the $\text{H}\alpha$ luminosity and consequently of the Star Formation Rate (SFR). In this respect, a spatially resolved 2D determination of the extinction is essential for a proper characterization of the stellar populations and the star formation history of Mrk 409, and more in general of BCD galaxies.

In computing the extinction map, we corrected the $\text{H}\beta$ line for underlying stellar absorption by fitting a Gaussian profile to its absorption wings. For the $\text{H}\alpha$ line, the absence of absorption wings makes a reliable decomposition impossible. In this case, in principle several approaches could be adopted : a) to take for $\text{H}\alpha$ the same value in absorption that for $\text{H}\beta$, that is, to set $\text{EW}(\text{H}\alpha_{\text{abs}}) = \text{EW}(\text{H}\beta_{\text{abs}})$, traditionally the most common strategy; b) to apply spectral synthesis models to disentangle the young and old population spectra and, from the model output, estimate the $\text{EW}(\text{H}\alpha)$ in absorption; c) to assume that the absorption in $\text{H}\alpha$ is negligible.

Taking into account that both a) and b) rest on "model-dependent" values, probably overestimations of the underlying absorption in $\text{H}\alpha$, which in turn overestimates $C_{\text{H}\beta}$, we prefer to adopt the most conservative c) approach, keeping in mind that under this assumption the computed extinction value is a lower limit to the actual value.

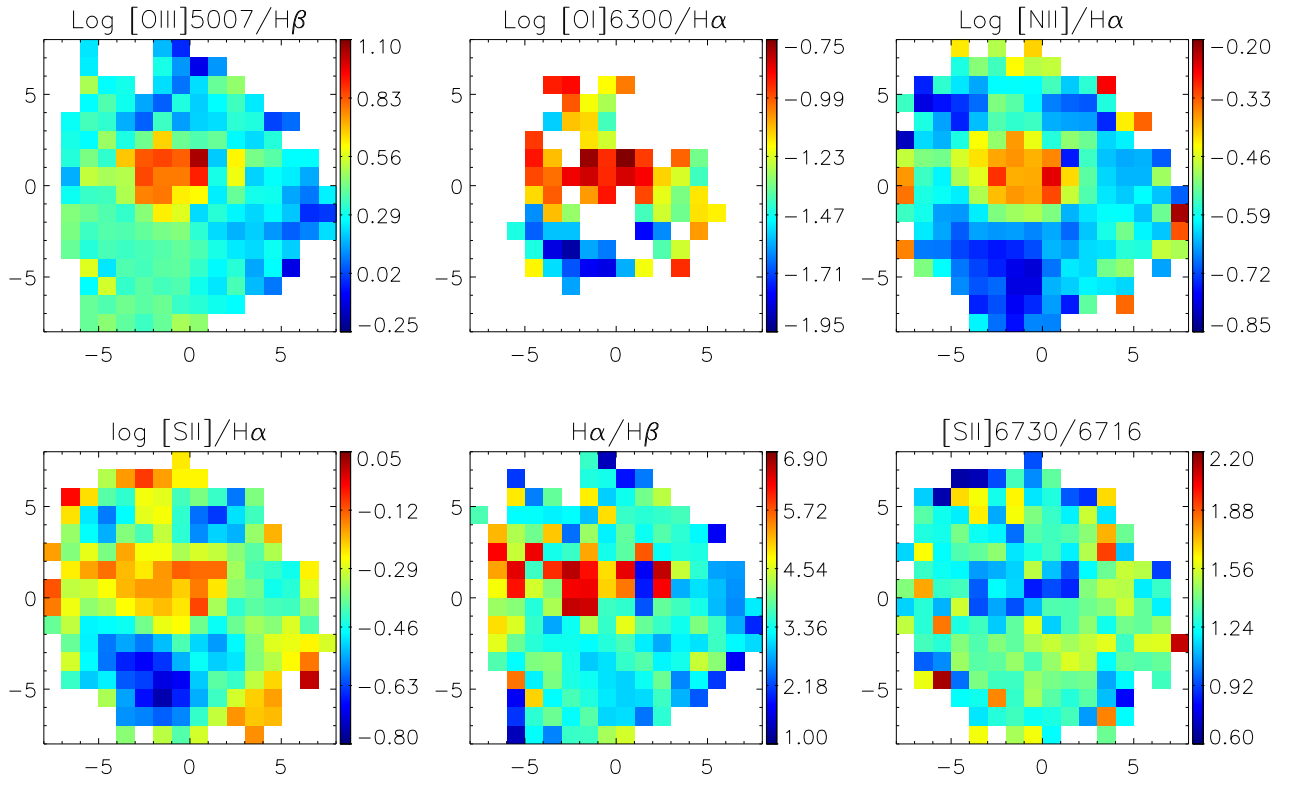


Fig. 3.— Ionization ratios (first four panels), interstellar extinction and electron density maps. Axis units are arcseconds; north is up, east to the left. Ionization ratio maps are in logarithmic scale.

3.3. Integrated spectroscopy of selected galaxy regions

As the next step in our analysis, we used the reconstructed flux and continuum maps to delimit the regions of interest in the galaxy. A total of six regions were identified, the five SF located in the ring and the nuclear SF region #3 (see Fig. 1).

We identified the spaxels corresponding to each of these regions, and summed their spectra together to create the integrated spectrum. In this way we produce higher signal-to-noise spectra (in comparison to the spectra of the individual spaxels), better suited for the derivation of physical parameters and chemical abundances.

In Figure 4 we compare the flux-calibrated spectra of these regions, prior to correction for interstellar extinction. The spectra are arbitrarily shifted on the vertical axis, for the sake of clarity. It can be seen that the spectral energy distribution (SED) of the nucleus #3 differs strikingly from that in regions along the circumnuclear SF ring (#1, #2, #4–6). In the nuclear starburst the stellar continuum is an order of magnitude higher than in the ring; it displays prominent absorption features, including the higher-order Balmer lines, $H\delta$ and $H\gamma$, CaII H and K lines, NaI $\lambda 5922$ or the G-band at $\lambda 4304$. Its strong [O I] $\lambda 6300$ emission is also remarkable, suggesting an additional contribution to the ionization, other than photoionization from OB stars. This comparatively red stellar continuum and the strong absorption features both indicate that the emission is dominated by older stars. The SF regions in the ring display, on contrast, an almost flat continuum with stronger emission lines, such as [O II] $\lambda 3727$, $H\beta$, [O III] $\lambda 5007$, $H\alpha$, [N II] $\lambda \lambda 6548, 6584$ and [S II] $\lambda \lambda 6717, 6731$, in addition to weak [O I] $\lambda 6300$ emission. These spectra also reveal absorption wings in $H\delta$ and $H\gamma$ and such absorption features as CaII H K $\lambda \lambda 3933, 3969$.

We measured the fluxes and equivalent widths of the most prominent emission lines in each spectrum. The extinction in each region was determined from the $H\alpha/H\beta$ ratio, as the measured $H\delta$ and $H\gamma$ fluxes are doubtful due to their intrinsic weakness and the large uncertainties in the correction for the underlying stellar absorption. For the theoretical $H\alpha/H\beta$ value, we adopted the case B Balmer recombination decrement $H\alpha/H\beta = 2.86$ for $T = 10000$ K and $N_e = 10^4$ cm $^{-3}$ (Brocklehurst 1971); the Whitford (1958) reddening curve as parametrized for Miller & Mathews (1972) was used.

For $H\beta$, where absorption wings are clearly resolved, we fitted simultaneously an absorption and an emission component, in order to obtain precise measurements of the $H\beta$ flux in emission; however, in $H\alpha$, the absence of absorption wings makes a reliable decomposition impossible. Again, we assume that the absorption in $H\alpha$ is negligible, so that the derived $C_{H\beta}$ are actually lower limits.

For comparison, we also tabulate the values obtained by setting $EW(H\alpha_{\text{abs}}) = 2$ Å, as

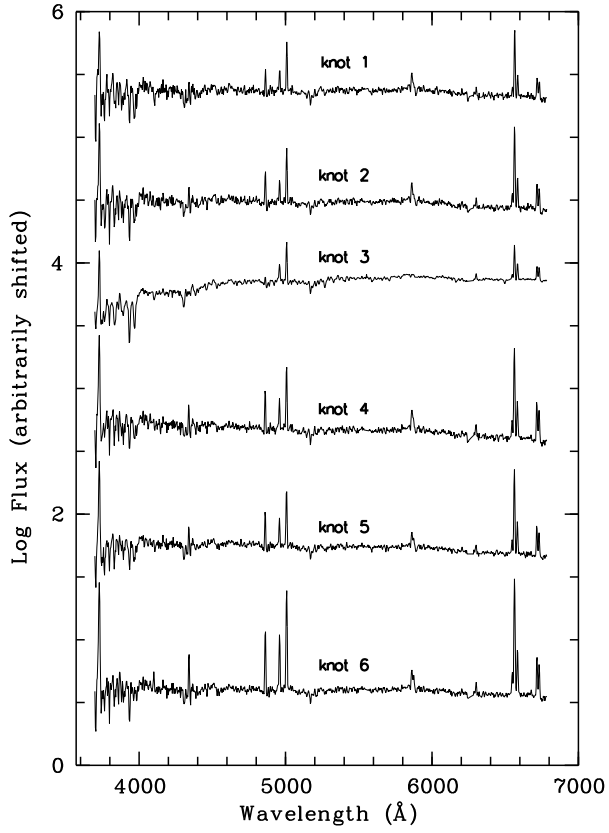


Fig. 4.— Flux-calibrated spectra of the six resolved star-forming regions in Mrk 409. The spectra are shown in logarithmic scale and are offset for the sake of clarity.

in the output spectra from the synthesis models run in Sect. 4, we measured an $\text{EW}(\text{H}\alpha_{\text{abs}})$ of about 1.5–2 Å. For this latter case we see a modest increase in the extinction coefficient.

The reddening corrected line intensities in each region are listed in Table 2. The most relevant line ratios are shown in Table 3.

The $\text{H}\alpha$ flux emitted by the SF regions is about 60% of the total $\text{H}\alpha$ flux within the PMAS field of view.

3.3.1. *Constraining the Ionization Mechanism*

The ionization mechanisms acting in a galaxy and their spatial distribution can be studied by means of the line ratio diagrams for the usual diagnostic lines (Baldwin et al. 1981; Veilleux & Osterbrock 1987). These diagnostic diagrams help distinguish among the different ionization mechanisms (photoionization from young stars, photoionization by a power law continuum source and shock-wave heating) operating in a galaxy.

The position of the six regions under study on the diagnostic diagram $[\text{O III}] \lambda 5007/\text{H}\beta$ vs $[\text{O I}] \lambda 6300/\text{H}\alpha$, $[\text{N II}] \lambda 6584/\text{H}\alpha$ and $[\text{S II}] \lambda\lambda 6717, 6731/\text{H}\alpha$ is shown in Figure 5. The empirical boundaries between the different zones (from Veilleux & Osterbrock 1987), as well as the theoretical boundaries proposed by Kewley et al. (2001), are also plotted.

H II-like ionization (i.e. star formation) seems to be the dominant mechanism in the five SF knots conforming the ring (see also Table 3 for the specific values of the emission line ratios). The line ratios of the nuclear region #3, however, are consistent with those of Seyfert galaxies. We came to the same conclusion assuming an extreme correction for the underlying $\text{H}\alpha$ absorption of $\text{EW}(\text{H}\alpha_{\text{abs}}) = 4$ Å for the nuclear region. The possibility of the nuclear region of Mrk 409 containing a non-thermal energy source cannot be discarded. Indirect evidence for this interpretation comes from the failure of purely stellar synthetic spectra to reproduce the observed spectrum of that region (see Sect. 4).

3.3.2. *Physical parameters and chemical abundances*

The physical properties and oxygen abundances for Mrk 409 are listed in Table 3.

The electron density (N_e) for the individual SF knots was derived from the $[\text{S II}] \lambda\lambda 6717, 6731$ Å line ratio using the task TEMDEN in the IRAF NEBULAR package (De Robertis et al. 1987; Shaw & Dufour 1995).

Table 2. Reddening corrected line intensity ratios

Line (Å)	Ion	Knot #1		Knot #2		Knot #3		Knot #4		Knot #5		Knot #6	
		F_λ	$-W_\lambda$	F_λ	$-W_\lambda$	F_λ	$-W_\lambda$	F_λ	$-W_\lambda$	F_λ	$-W_\lambda$	F_λ	$-W_\lambda$
3727	[O II]	5.06 ± 1.18	40.3 ± 2.9	4.29 ± 0.80	46.8 ± 2.6	13.13 ± 2.61	25.5 ± 0.7	4.84 ± 0.62	52.3 ± 1.8	5.03 ± 0.68	47.0 ± 1.9	3.50 ± 0.34	86.1 ± 1.2
4861	H β	1.00 ± 0.00	5.4 ± 0.7	1.00 ± 0.00	7.9 ± 0.8	1.00 ± 0.00	1.4 ± 0.2	1.00 ± 0.00	9.1 ± 0.5	1.00 ± 0.00	7.4 ± 0.5	1.00 ± 0.00	18.6 ± 0.3
4959	[O III]	0.89 ± 0.15	5.2 ± 0.4	0.48 ± 0.07	3.9 ± 0.4	2.51 ± 0.34	3.8 ± 0.1	0.61 ± 0.05	5.9 ± 0.3	0.74 ± 0.07	6.0 ± 0.4	0.79 ± 0.03	14.3 ± 0.2
5007	[O III]	2.13 ± 0.30	12.6 ± 0.4	1.64 ± 0.18	13.7 ± 0.4	5.68 ± 0.76	8.9 ± 0.1	1.89 ± 0.12	18.6 ± 0.4	1.98 ± 0.14	16.3 ± 0.4	2.36 ± 0.07	43.4 ± 0.4
6300	[O I]	0.20 ± 0.06	1.3 ± 0.3	0.16 ± 0.03	1.5 ± 0.2	0.44 ± 0.09	1.0 ± 0.1	0.18 ± 0.03	2.1 ± 0.3	0.17 ± 0.03	1.7 ± 0.3	0.10 ± 0.01	2.0 ± 0.3
6548	[N II]	0.25 ± 0.07	1.7 ± 0.3	0.25 ± 0.05	2.5 ± 0.3	0.40 ± 0.09	1.0 ± 0.1	0.27 ± 0.03	3.3 ± 0.3	0.25 ± 0.03	2.6 ± 0.2	0.21 ± 0.01	4.5 ± 0.2
6563	H α	2.86 ± 0.55	19.7 ± 0.4	2.86 ± 0.43	28.9 ± 0.6	2.86 ± 0.52	7.5 ± 0.1	2.86 ± 0.24	35.6 ± 0.6	2.86 ± 0.27	29.9 ± 0.4	2.86 ± 0.12	60.1 ± 0.3
6584	[N II]	0.58 ± 0.13	4.0 ± 0.3	0.62 ± 0.10	6.2 ± 0.4	1.19 ± 0.22	3.1 ± 0.1	0.67 ± 0.06	8.3 ± 0.3	0.62 ± 0.06	6.4 ± 0.3	0.53 ± 0.02	6.4 ± 0.3
6717	[S II]	0.58 ± 0.13	4.2 ± 0.4	0.49 ± 0.08	5.1 ± 0.3	0.89 ± 0.17	2.5 ± 0.1	0.67 ± 0.06	8.8 ± 0.3	0.57 ± 0.06	6.2 ± 0.4	0.40 ± 0.02	0.0 ± 0.4
6731	[S II]	0.44 ± 0.10	3.2 ± 0.3	0.35 ± 0.06	3.7 ± 0.3	0.86 ± 0.16	2.4 ± 0.1	0.51 ± 0.05	6.7 ± 0.4	0.39 ± 0.05	4.3 ± 0.3	0.30 ± 0.02	0.0 ± 0.3
$C_{H\beta}$		0.23 ± 0.19		0.22 ± 0.14		0.91 ± 0.18		0.21 ± 0.08		0.27 ± 0.09		0.21 ± 0.04	
$C_{H\beta}^*$		0.35 ± 0.19		0.30 ± 0.14		1.23 ± 0.18		0.27 ± 0.08		0.35 ± 0.09		0.22 ± 0.04	
$F(H\beta)$		1.74 ± 0.84		2.51 ± 0.94		18.27 ± 8.91		4.09 ± 0.86		3.63 ± 0.87		17.27 ± 1.74	

Note. — Reddening-corrected line intensities, normalized to $F(H\beta) = 1$, for the individual regions selected in Mrk 409. The reddening coefficient, $C_{H\beta}$, and the corrected H β flux, $F(H\beta)$ ($\times 10^{-15}$ ergs cm $^{-2}$ s $^{-1}$), were computed assuming no underlying H α absorption. For comparison, we also list $C_{H\beta}^*$, the reddening coefficient derived by assuming $EW(H\alpha_{abs}) = 2 \text{ \AA}$.

16

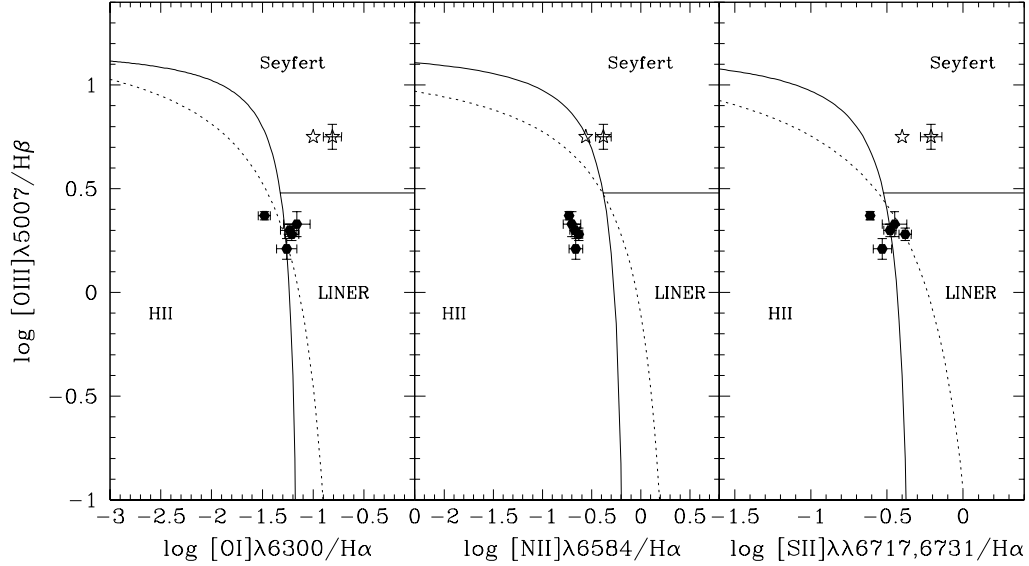


Fig. 5.— Optical emission-line diagnostic diagrams, separating Seyfert galaxies and LINERs from H II region-like objects. Solid lines are the empirical borders from Veilleux & Osterbrock (1987), while dotted lines are the theoretical borders from Kewley et al. (2001). The line ratios for the nuclear SF region of Mrk 409 (#3) and the five circumnuclear SF regions (#1–2 and #4–6) are plotted with open and filled symbols, respectively. For the nuclear region, we also mark (open star without errorbar) the position corresponding to assuming a correction for underlying $\text{H}\alpha$ absorption of $\text{EW}(\text{H}\alpha_{\text{abs}}) = 4 \text{ \AA}$ (for all other knots, this shift would be unnoticeable). Note that, in all three classification diagrams, the nuclear SF region falls in the Seyfert regime.

The "direct" oxygen abundance method relies on measurements of temperature-sensitive auroral lines (usually [O III] $\lambda 4363$), which are weak and often not detected in oxygen-rich systems (above $\sim 12 + \log(\text{O}/\text{H}) = 8.3 - 8.4$). This is the case of the spectra of Mrk 409, in which either we fail to detect the [O III] $\lambda 4363$ emission line, or, in the cases where we do detect the [O III] $\lambda 4363$ line, the S/N is too low for a reliable flux determination.

Different empirical and theoretical metallicity calibrations have been devised over the past two decades as an alternative for estimating oxygen abundances without any direct electron temperature measurements (Pagel et al. 1979; Alloin et al. 1979; Edmunds & Pagel 1984; McGaugh 1991; Vilchez & Esteban 1996; Pettini & Pagel 2004; Pilyugin et al. 2006). These calibrations are referred to as strong-line methods since they are based on ratios built on strong emission lines ([O II] $\lambda 3727$, [O III] $\lambda\lambda 4959, 5007$, [N II] $\lambda 6584$, [S II] $\lambda\lambda 6717, 6731$, [S III] $\lambda\lambda 9069, 9532$). We have used the strong-line methods from McGaugh (1991)[hereafter M91] and Pettini & Pagel (2004)[hereafter PP04] to derive the oxygen abundances of all selected SF knots, except the nuclear region #3 (see below).

Efforts have been made to refine the calibration of the R_{23} parameter. One of the most successful is the calibration by M91, which is based on photoionization models — the analytic expressions for the M91 theoretical models can be found in Kobulnicky, Kennicutt & Pizagno (1999). This calibration can be as precise as 0.2 dex (Kobulnicky, Kennicutt & Pizagno 1999). However, due to the well-known double-valued behavior between R_{23} and O/H, this method requires some prior knowledge of the galaxy's metallicity, in order to place it on the correct branch of the curve. We used the ratio [N II] $\lambda 6584/\text{H}\alpha$ to break the R_{23} degeneracy; in all the SF regions, $\log([\text{N II}] \lambda 6584/\text{H}\alpha)$ is > -1.1 , indicating that the knots lie on the upper branch — the division between the R_{23} upper and lower branches takes place between $-1.3 < \log([\text{N II}] \lambda 6584/\text{H}\alpha) < -1.1$ (Kewley & Ellison 2008).

On the other hand, PP04 revised the N2 ($\text{N2} \equiv \log([\text{N II}] \lambda 6584/\text{H}\alpha)$) and O3N2 ($\text{O3N2} \equiv \log([\text{O III}] \lambda 5007/\text{H}\beta/[\text{N II}] \lambda 6584/\text{H}\alpha)$) indices, using 137 extragalactic HII regions. The uncertainties in metallicity determinations based on these calibrations amount to ~ 0.38 and 0.25 dex, respectively.

Inspection of Fig. 5 shows knot #3 to be located in the Seyfert zone of the diagnostic diagram. For this region, we estimate therefore the metallicity using the chemical abundance calibrations proposed by Storch-Bergmann et al. (1998). These calibrations were derived for the range $8.4 \leq 12 + \log(\text{O}/\text{H}) \leq 9.4$ and tested using a sample of Seyfert galaxies and LINERs that have H II regions in the vicinity of their nucleus.

Table 3. Line ratios, physical parameters and chemical abundances

Parameter	Knot #1	Knot #2	Knot #3	Knot #4	Knot #5	Knot #6
$\log\left(\frac{[\text{O III}]_{\lambda 5007}}{\text{H}\beta}\right)$	0.33 ± 0.06	0.22 ± 0.05	0.75 ± 0.06	0.28 ± 0.03	0.30 ± 0.03	0.37 ± 0.02
$\log\left(\frac{[\text{N II}]_{\lambda 6584}}{\text{H}\alpha}\right)$	-0.70 ± 0.09	-0.66 ± 0.07	-0.38 ± 0.08	-0.63 ± 0.04	-0.67 ± 0.05	-0.73 ± 0.03
$\log\left(\frac{[\text{S II}]_{\lambda\lambda 6717, 6731}}{\text{H}\alpha}\right)$	-0.45 ± 0.08	-0.53 ± 0.06	-0.21 ± 0.07	-0.38 ± 0.04	-0.48 ± 0.04	-0.61 ± 0.02
$\log\left(\frac{[\text{O I}]_{\lambda 6300}}{\text{H}\alpha}\right)$	-1.16 ± 0.13	-1.26 ± 0.10	-0.81 ± 0.09	-1.21 ± 0.07	-1.23 ± 0.09	-1.46 ± 0.06
N_e	117	≤ 100	516	102	≤ 100	≤ 100
$12 + \log(\text{O}/\text{H})^a$	8.40	8.45	...	8.44	...	8.38
$12 + \log(\text{O}/\text{H})^b$	8.46	8.49	...	8.51	8.48	8.43
$12 + \log(\text{O}/\text{H})^c$	8.40	8.53	...	8.45	8.42	8.54
$12 + \log(\text{O}/\text{H})^d$	8.44
$\log(\text{N}/\text{O})^e$	-1.13	-1.02	-1.28	-1.05	-1.11	-1.01

Note. — The line ratios have been corrected for galactic extinction. The quoted uncertainties include both measurement errors and the uncertainty in the calibration factor. (a) Oxygen abundances computed using the fit to the relationship between T_e metallicities and the $([\text{O III}]/\text{H}\beta)/([\text{N II}]/\text{H}\alpha)$ in Pettini & Pagel (2004); (b) oxygen abundances obtained from the relationship between T_e metallicities and the $[\text{N II}]/\text{H}\alpha$ ratio given by Pettini & Pagel (2004); (c) oxygen abundances derived using the McGaugh (1991) calibration for the upper branch; (d) oxygen abundance computed from chemical abundance calibrations for Seyfert galaxies (Storchi-Bergmann et al. 1998); (e) $[\text{N II}]/[\text{O II}]$ was used to obtain the N/O abundance ratio (Pérez-Montero & Díaz 2005).

3.4. Kinematics of the ionized gas

Figure 6 shows the velocity field of the ionized gas, derived from the [O III] $\lambda 5007$ and the H α emission lines. Both velocity maps show essentially the same regular pattern, although in the [O III] $\lambda 5007$ map it appears slightly more distorted; the galaxy displays an overall smooth rotation pattern along a northwest-southeast axis.

Figure 7 shows the velocity profile and the position angle of the kinematical axis, as determined by a tilted-ring analysis of the H α velocity field based on the *kinemetry* method developed by Krajnović et al. (2006).

The velocity rises rapidly in the inner 4 arcsecs, then flattens out at about 60 km s^{-1} . Adopting for simplicity the virial formula valid for spherical symmetry, we can estimate the mass from the relation: $M(R) = 2.32 \times 10^5 R v_{\text{circ}}^2(R)$ (Lequeux 1983), where R is in kpc, $v_{\text{circ}} = v_{\text{obs}}/\sin(i)$ is the circular velocity, i is the inclination angle, and M is expressed in solar units.

The apparent flattening of Mrk 409 is $q = b/a \simeq 0.80$ (SDSS, Data Release 6), which, for an intrinsic flattening $q_{\text{intr}} \lesssim 0.3$ gives an inclination angle $i \simeq 38$. Taking an observed rotational velocity $v \simeq 60 \text{ km s}^{-1}$ at the position of the SF ring, we obtain an indicative virial mass of $\simeq 1.4 \times 10^9 M_{\odot}$ interior to the SF ring ($R_{\text{ring}} \approx 0.6 \text{ kpc}$).

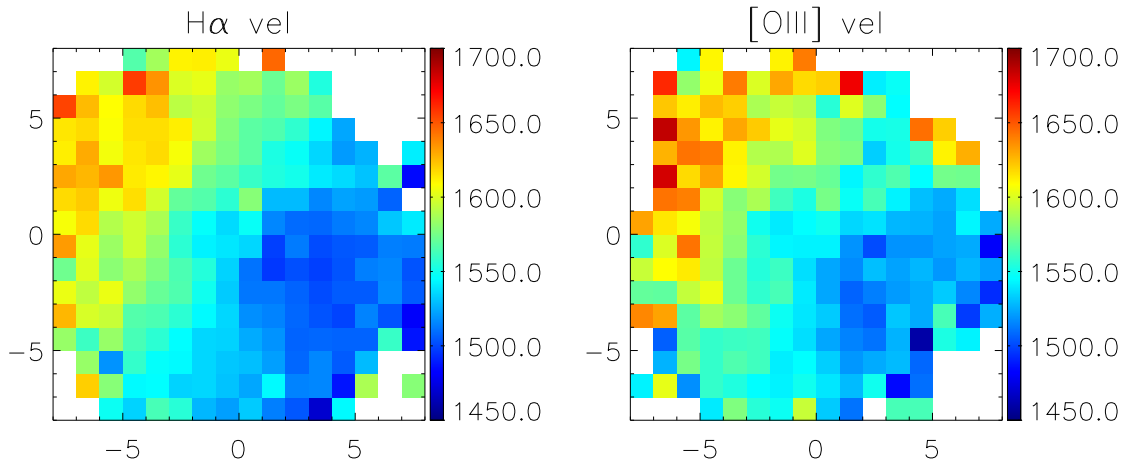


Fig. 6.— Velocity field of the ionized gas in the central region of Mrk 409 in the [O III] and H α lines. Axis units are arcseconds; north is up, east to the left.

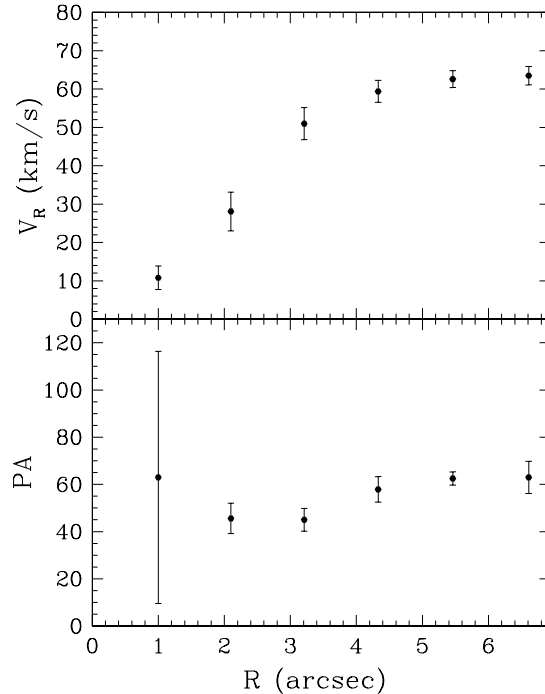


Fig. 7.— Velocity curve and position angle profile of the kinematical major axis (measured from north through east) as determined by a tilted-ring model analysis.

4. Discussion

As it was already stated in the introduction, one of the main open questions in BCD research is how the star formation originates and propagates across these galaxies. The spatial distribution of the SF knots in the central part of Mrk 409 — a nuclear starburst surrounded by a SF ring — makes this galaxy a paradigm case of study.

An extended circumnuclear SF zone may play an important role on BCD evolution, contributing to the build-up of the stellar component and to the chemical enrichment of the Interstellar Medium (ISM). In addition, the possibility of Mrk 409 hosting a non-thermal nuclear energy source (see Sect. 3.3.1), makes this object even more intriguing. In this line, Izotov & Thuan (2008) reported recently on the detection of AGN candidates in four metal-poor dwarf galaxies, and circumnuclear SF activity is known to exist in several AGNs hosted by normal galaxies (Wilson et al. 1986; Kotilainen et al. 2000;

González Delgado et al. 2001).

GdP03 suggested that the SF ring in Mrk 409 could have been formed as the result of the interaction of a starburst-driven shock with the surrounding ISM. These authors performed echelle spectroscopy of the central part of Mrk 409 and found a doubly-peaked H α emission line profile, with its two peaks shifted by -54 ± 3 and 37 ± 3 km s $^{-1}$ relative to the systemic velocity of the stars (presumably because of the lower spectral resolution, we do not see this feature in our spectra). But their data, covering only a thin slice of the BCD's central part, did not allow to firmly validate this scenario.

This idea appears also viable from the viewpoint of observational and theoretical work that indicates that BCDs experience multiple bursts of star formation in their central part through their lifetimes (e.g. Krüger & Fritze-v. Alvensleben 1994; Mas-Hesse & Kunth 1999). The mechanical energy released by the collective action of stellar winds from massive stars and SNe can readily result in large-scale expansive motions in the ISM reflected on e.g. H α super-shells out to kpc scales from the starburst region (Meurer et al. 1992; Marlowe et al. 1995; Cairós et al. 2001). Observations of BCDs indicate expansive velocities between a few 10 km s $^{-1}$ (see e.g. Meurer et al. 1992; Marlowe et al. 1995; Martin 1997; van Eymeren et al. 2007) and $\gtrsim 200$ km s $^{-1}$ (He 2-10, Papaderos & Fricke 1999; Johnson et al. 2000; Haro 2, Legrand et al. 1997).

An alternative hypothesis, which must also be taken into account, is that the ring found in Mrk 409 is a resonance ring (RR), similar to those observed in barred galaxies (Buta 1988; Buta & Purcell 1998; Kotilainen et al. 2000). RRs are thought to result from efficient gas inflow onto the central region of a galaxy, driven by the bar (Combes & Gerin 1985), and its collapse at the radius of the inner Lindblad resonance. While RRs are typically observed in galaxies of normal mass, they may as well exist in lower-mass systems, such as Mrk 409. Note that the gas-phase metallicity in the SF ring in Mrk 409 is in the range of values determined in circumnuclear SF regions in normal galaxies (Diaz et al. 2007), and also that the SF ring compares well in size ($R \sim 600$ pc) with RRs in normal galaxies – the average radius of galactic RRs is 750 pc (Buta & Crocker 1993) with values as small as ~ 200 pc (Comeron et al. 2009).

In order to distinguish between the two aforementioned scenarios it is important to study the SFH of the individual knots along the ring. In the framework of the RR hypothesis, it is reasonable to assume that this feature has been stable over several orbital periods (a few 10^8 yr), forming stars at a nearly constant rate, whereas the blast wave hypothesis, on the other hand, requires that the SF ring as a whole was created nearly instantaneously in the recent past.

Our PMAS data, mapping the nucleus and the SF ring, permit, despite their moderate spectral resolution, the investigation of this issue. In order to constrain the SFH of each SF knot, we interpret their integrated spectrum (Section 3.3) by means of spectral synthesis models. To check the consistency of our results, we use both the population synthesis code STARLIGHT (Cid Fernandes et al. 2004, 2005a,b; Garcia-Rissmann et al. 2005) and the evolutionary spectral synthesis code PEGASE (Fioc & Rocca-Volmerange 1997).

We use STARLIGHT to synthesize the observed stellar continuum in each SF region as due to the superposition of single-age stellar populations (SSPs) of different ages and metallicities. The SSP library used is based on stellar models by Bruzual & Charlot (2003) for a Salpeter *initial mass function* (IMF), five metallicities (between $Z_{\odot}/50$ and $2.5 Z_{\odot}$) and 59 ages (between 1 Myr and 13 Gyr). Prior to modelling, the observed spectra were corrected for interstellar extinction (using the $C_{H\beta}$ derived without stellar absorption correction in $H\alpha$), and spectral regions containing strong emission lines or skyline subtraction residuals were flagged out.

Fig. 8 (top panel) displays the extinction-corrected spectra of the circumnuclear SF regions #1, #2 and #4–6, normalized at 4200 \AA (orange color) together with the best-fitting synthetic spectra overlaid in black. Flagged intervals in each spectrum are marked with shaded vertical bars. The smaller panels to the upper-right and lower-right show the age distribution of the SSPs selected by STARLIGHT as a function of, respectively, their luminosity and mass fraction in %. We find that the spectra of all circumnuclear regions are well fit by the superposition of a several Gyr old stellar component with a young (<50 Myr) population which dominates the optical light. In none of the regions do STARLIGHT models indicate an intermediate-age stellar population bridging the gap between 0.1 and ~ 1 Gyr. All solutions imply no or little ($A_V \leq 0.14$ mag) intrinsic extinction in excess to that inferred from the measured $C_{H\beta}$. According to the fits, the formation of the underlying host galaxy of Mrk 409 was accomplished between ~ 1 and ~ 10 Gyr ago, and at least 3/4 of its stellar mass was at place ~ 6 Gyr ago. This is in good agreement with the red $B-R$ color of ~ 1.1 mag of the host of Mrk 409 (GdP03).

Secondly, we apply a modified version of PEGASE 2.0 to study whether the SFH along the ring is better approximated by an instantaneous or a continuous model (models `inst` and `c0-c2`, respectively, in Table 4). In this approach, each of the observed spectra is modeled as due to the superposition of the SED of an old and a young stellar population describing, respectively, the underlying old host galaxy and the SF ring. We use the same input spectra as for STARLIGHT after resampling to the lower spectral resolution of PEGASE. We furthermore assume a Salpeter IMF between 0.1 and $100 M_{\odot}$ and a fixed stellar metallicity of $Z_{\odot}/5$. For the old underlying population we adopt an exponential SFR with an e-folding

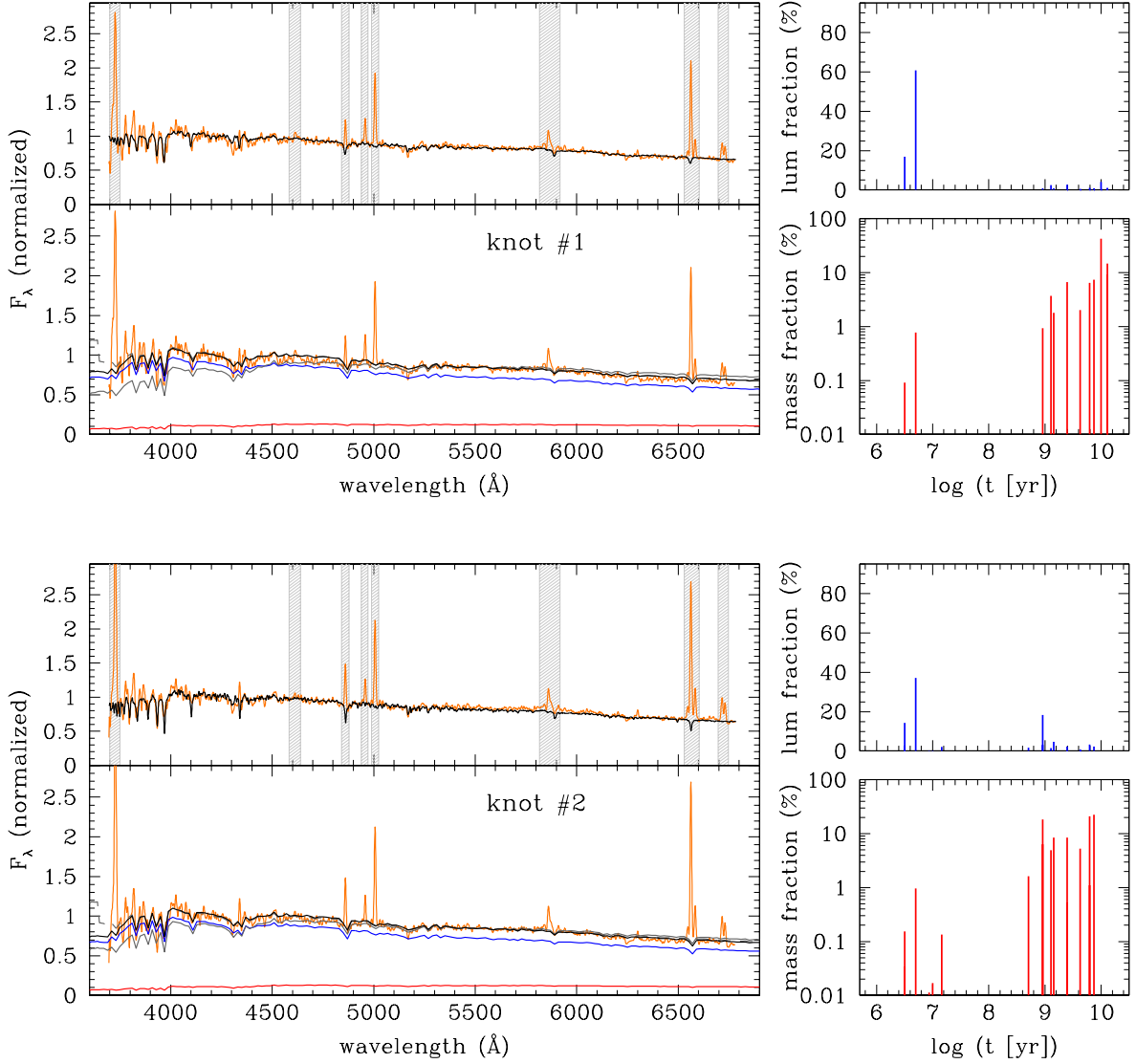


Fig. 8.— Spectra of the five selected regions in the circumnuclear star-forming ring in Mrk 409, corrected for extinction and normalized by the observed flux at 4200 Å (orange color). The spectra are arranged from region #1 (top) to region #6 (bottom). The best-fitting synthetic spectral energy distribution (SED) for the stellar continuum, calculated with the population synthesis code STARLIGHT (Cid Fernandes et al. 2005a), are shown in the upper panel in black. Flagged intervals are marked with shaded vertical bars. The smaller upper-right and lower-right panels show the age distribution of the stellar populations in the synthetic SEDs as a function of, respectively, their luminosity (at 4200 Å) and mass contribution in %. The SEDs corresponding to the best-fitting Pegase 2.0 models *inst*, *c0* and *c1* are shown in the lower panel with the black, solid-gray and dashed-gray curve, respectively. The blue and red curves illustrate the young and old stellar component, as derived from the *inst* model.

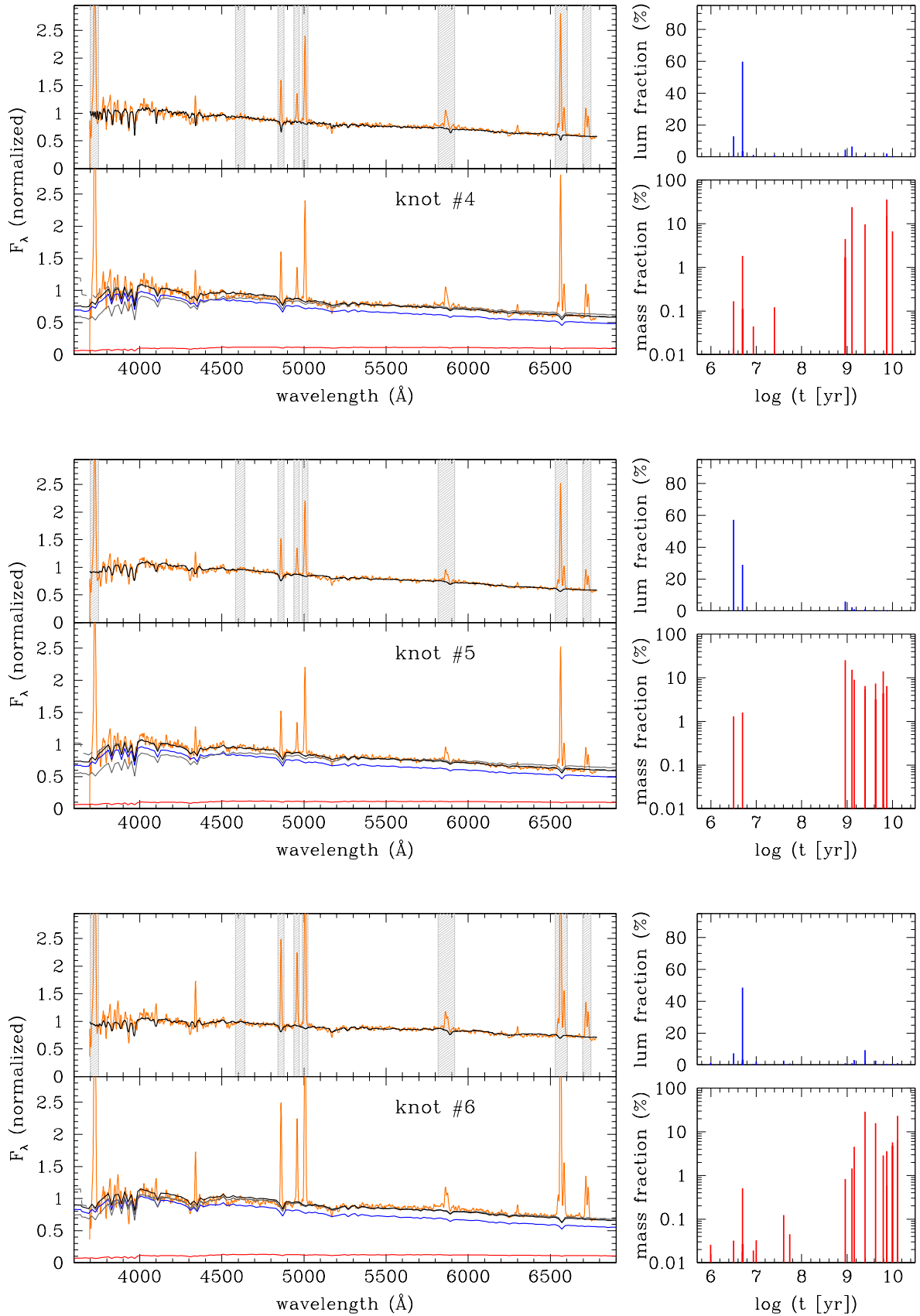


Fig. 8.— Continued.

time $\tau = 3$ Gyr, except for model **c2** for which τ was set to 1 Gyr. For these two e-folding times the observed B - R color of the host galaxy is reproduced by a present age of 10.3 Gyr and 5 Gyr, respectively. Models **inst** and **c0** fit both the stellar SED and the observed EWs of the $H\alpha$ and $H\beta$ emission lines whereas in models **c1** and **c2** only the stellar SED was fitted.

The results for each SF region are summarized in Table 4. The age and mass of the young stellar component t_{SF} and $M_{\star, \text{SF}}$ are given in cols. 3 and 4, respectively. Columns 5 and 6 list the predicted EWs of the $H\alpha$ and $H\beta$ emission line and $B - R$ color. Column 7 gives the difference $\Delta\mu_B$ between the B -band surface brightness of the old stellar population and that of the total stellar population predicted by the fit ($\mu_{B, \text{old}} - \mu_{B, \text{total}}$), and col. 8 the reduced χ^2 . The observed EWs of the $H\alpha$ and $H\beta$ lines are also indicated for each SF region.

The best-fitting stellar SEDs for each circumnuclear region, overlaid with the observed spectrum, are shown in Fig. 8 (bottom panel). The SEDs corresponding to models **inst**, **c0** and **c1** are shown with the black, solid-gray and dashed-gray curve, respectively. The blue and red curves illustrate the young and old stellar component, as derived from the **inst** model.

Inspection of Table 4 and Fig. 8 shows that the instantaneous model reproduces best both the stellar SED and the EW of $H\alpha$ and $H\beta$, implying in all cases a burst age t_{SF} of 6 to 10 Myr. The predicted stellar mass from this model adds up to $\sim 1.5 \times 10^6$. Models **c0**, assuming continuous star formation since t_{SF} (in most cases ≥ 2 Gyr), generally fail to simultaneously reproduce both the EWs and the stellar SED, with a clear tendency for underestimating the latter for $\lambda < 4500$ Å. Continuous SF models fitting the stellar SED only (**c1** and **c2**) predict, similar to the instantaneous model, a young age, however, they strongly overestimate the EWs of $H\alpha$ and $H\beta$. Comparison of models **c1** and **c2** shows that the adopted e-folding time for the host galaxy has a minor effect on t_{SF} .

Table 4. Model results for each SF region

Region	Model	t_{SF}	$M_{*,\text{SF}}$ ($10^6 M_{\odot}$)	EW(H α) Å	EW(H β) Å	$B - R$ (mag)	$\Delta\mu_B$ (mag)	χ^2
1	inst	10 Myr	0.27	20	5	0.82	0.62	0.044
	c0	2.5 Gyr	1.46	23	7	1.05	0.17	0.389
	c1	7 Myr	0.11	296	78	0.84	0.74	0.029
	c2	10 Myr	0.09	237	61	0.82	0.75	0.032
	obs			19.7	5.4			
2	inst	8 Myr	0.17	28	7	0.80	0.60	0.047
	c0	2.5 Gyr	2.8	34	10	0.96	0.42	0.218
	c1	7 Myr	0.11	292	77	0.84	0.73	0.024
	c2	10 Myr	0.09	235	60	0.82	0.74	0.025
	obs			28.9	7.9			
3	inst	44 Myr	37.4	7	2	0.60	1.48	0.227
	c0
	c1	2 Gyr	49.1	108	24	0.56	2.9	0.121
	c2	1 Gyr	47.3	112	25	0.57	1.9	0.125
	obs			7.5	1.4			
4	inst	8 Myr	0.27	33	8	0.70	0.80	0.085
	c0	2.5 Gyr	4.8	44	12	0.89	0.64	0.374
	c1	10 Myr	0.19	326	80	0.75	0.97	0.031
	c2	20 Myr	0.20	248	60	0.73	0.97	0.033
	obs			35.6	9.1			
5	inst	8 Myr	0.28	31	8	0.73	0.74	0.053
	c0	3 Gyr	4.4	36	10	0.95	0.47	0.380
	c1	30 Myr	0.38	197	49	0.76	0.86	0.025
	c2	17 Myr	0.18	241	60	0.76	0.89	0.024
	obs			29.9	7.4			
6	inst	6 Myr	0.47	55	14	0.76	0.62	0.092
	c0	0.45 Gyr	3.7	65	17	0.84	0.63	0.067
	c1	7 Myr	0.34	279	74	0.85	0.70	0.027
	c2	7 Myr	0.24	280	73	0.84	0.72	0.029
	obs			60.1	18.6			

Note. — Col. 1: Star forming region ID; col. 2: model; cols. 3, 4: age and mass of the young stellar component; cols 5, 6: predicted equivalent width of the H α and H β emission lines; col. 7: difference between the B -band surface brightness of the older stellar population and that of the total stellar population predicted by the fit; col. 8: reduced χ^2 of the fit. For each knot, the last line, labeled “obs”, shows the observed H α

and $H\beta$ equivalent widths.

In summary, both population and evolutionary spectral synthesis models argue independently against the idea that the SF ring in Mrk 409 is forming continuously with a constant SFR since several 10^8 yr, as expected from the RR scenario. Instead, they consistently point to a recent (~ 10 Myr) enhancement of the SFR in all circumnuclear SF regions.

Clearly, regardless of the model used, any conclusions related to the SFH of the ring should be considered with caution. It is known that both spectral synthesis approaches are plagued by ambiguities, especially when applied to complex emitting sources, such as starburst galaxies, involving multiple stellar populations of different age and metallicity, and being likely subject to different amounts of intrinsic extinction.

Solutions by STARLIGHT are guided by the minimal linear combination of age vectors, i.e. they discard out of the available library SSPs with a low significance. Aside from the degeneracy problem, the solutions may therefore provide a very fragmentary view of the true SFH in a galaxy. In our concrete case, the absence of SSPs in the age interval between ~ 40 Myr and ~ 1 Gyr should not be taken as foolproof of cessation of SF activities during that period, and the hypothesis of a low-level star formation in the ring cannot be rejected with certainty.

Evolutionary synthesis models suffer as well from ambiguities stemming not only from the age-metallicity degeneracy but, as thoroughly discussed in Guseva et al. (2001), by uncertainties in the intrinsic extinction and in the SFH assumed. The instantaneous and continuous model likely represent two extreme cases and rather poor approximations to the true SFH along the circumnuclear ring. For example, a continuous SF process over the last ~ 1 Gyr with a varying or recently elevated SFR may also match the observations. However, an investigation of more complex SFHs on the basis of the present data would likely not completely lift uncertainties in the interpretation of the SF ring.

We stress that the satisfactory agreement between the two conceptually different models used is reassuring. We are therefore confident in that an instantaneous burst is a better description of the SFH of the individual SF knots in the ring.

Furthermore, the morphology of the galaxy does not show any bar or non-axisymmetric features, conditions required for the formation of a galactic RR. In a recent paper, Comeron et al. (2009) note that Mrk 409 (NGC 3011) has no obvious bar, and place it into the group of galaxies that have “nuclear rings that cannot easily be explained in a resonance framework”.

Hence, both the synthesis models results and the galaxy morphology speak against the presence of a RR in this galaxy, and favor the starburst-driven shock scenario as the most plausible to explain the origin of the SF ring in Mrk 409.

The nature of the nuclear region #3 is puzzling. As discussed already, its observed line ratios suggest an additional non-thermal source. Further support to this interpretation comes from spectral synthesis models which both fail to reproduce its observed SED without large systematic residuals (cf. Fig. 9). Although inclusion of a power law component along with a variation in the extinction model might produce a better fit, we preferred not to do so, as this would probably not add solid constraints to the understanding of the nature and SFH of the nuclear region.

However, assuming that the luminosity of region #3 is dominated by stars, we can formally check whether its energetic output is consistent with the blast wave scenario. Taking its predicted burst age and total stellar mass of $t_{\text{SF}} \approx 44$ Myr and $M_{\star, \text{SF}} \approx 3.7 \times 10^7 M_{\odot}$ (Table 4) at face value, we estimate from STARBURST99 (Leitherer et al. 1999, their Fig. 111) the mean *mechanical* luminosity imparted to the ISM over t_{SF} via radiative winds and SNe to $\sim 3.8 \times 10^{41}$ erg s^{-1} . This modest mechanical luminosity, which is to be taken as an upper limit, can indeed readily produce a super-shell of the observed dimensions within a few Myrs.

From Eq. 2 of McCray & Kafatos (1987), the radius in pc of a shell writes as $R_s = 269(L_{38}/n_0)^{1/5} \cdot t_7^{3/5}$, where L_{38} denotes the mechanical luminosity in units of 10^{38} erg/s, $t_7 = t/(10^7 \text{ yr})$ and n_0 is the density of the ambient gas in cm^{-3} . For $L_{38} \sim 3800$ the radius of the starburst-driven shell at the age t_{SF} is $R_s \approx 3400/n_0^{1/5}$. Hence, the energetic output from the nuclear starburst region is sufficient for producing within $t \leq t_{\text{SF}}$ a super-shell with a R_s between ~ 600 pc (inner SF ring) and ~ 2.3 kpc (outer SF ring), depending on n_0 .

While the simple blast-wave scenario can formally be reconciled with the known properties of Mrk 409, a major open question pertains to the actual SFH of region #3.

While a conclusive assessment of this issue is out of reach with the present data, the co-evolution of a massive nuclear SF region and an AGN remains a viable and appealing interpretation for the overall characteristics of Mrk 409.

5. Conclusions

We presented PMAS integral field spectroscopy of the central $16'' \times 16''$ of the BCD galaxy Mrk 409. Mrk 409 is known to undergo intense SF activity within the central part of an old, elliptical host galaxy (Gil de Paz & Madore 2005). Previous work (GdP03) had revealed a compact (diameter $< 5''$) nuclear starburst region, surrounded by two nearly concentric rings of ionized gas emission with radii of 0.6 kpc and 2.8 kpc. The inner ring was proposed to be the result of in situ star formation in a dense shell of piled-up material

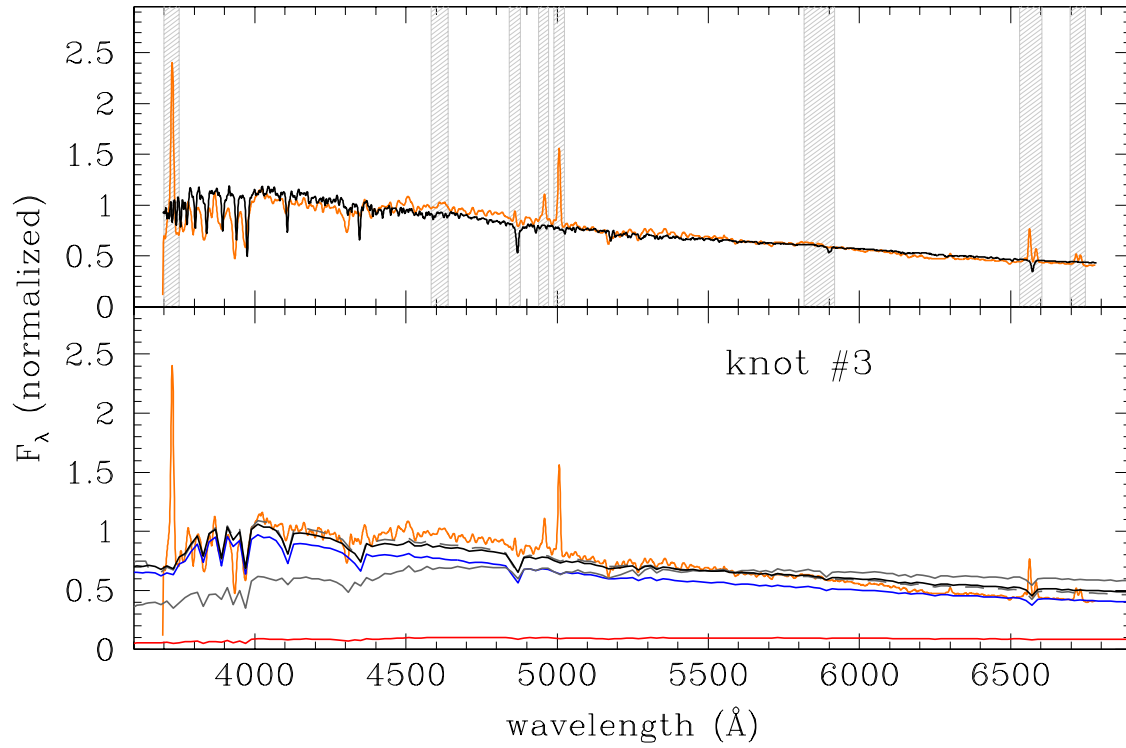


Fig. 9.— Observed and best-fitting synthetic spectrum with STARLIGHT (upper panel) and Pegase 2.0 (bottom panel) of the nuclear SF region #3. It can be seen from either diagram that a stellar population cannot fit the observed stellar continuum without systematic residuals.

on the surface of an expanding starburst-driven super-bubble.

The main results from the present study may be summarized as follows:

- The inner circumnuclear ring of Mrk 409 contains a young stellar population with a total mass of $\sim 1.5 \times 10^6 M_{\odot}$, which likely started forming almost coevally $\sim 10^7$ yr ago. This is strong evidence to the interpretation that circumnuclear SF activities in Mrk 409 were triggered through the collision of a spherically expanding, starburst-driven super-bubble with the ambient denser material. Although the details of this process remain unclear, our study suggests that sequential star formation in a spherical shell, as observed in Mrk 409, may contribute considerably to the build-up of the young stellar component in BCDs.
- While the circumnuclear SF ring presents properties typical of H II regions, diagnostic line ratios for the high-surface brightness starburst nucleus suggest an additional ionization source for this region, most probably a low-luminosity AGN.
- The nuclear and circumnuclear SF components in Mrk 409 also differ considerably in their extinction properties: SF regions in the ring show a moderate and relatively uniform intrinsic extinction ($0.2 \lesssim C_{H\beta} \lesssim 0.3$), while the nuclear emission is subject to strong dust obscuration ($C_{H\beta} \approx 0.9$). Consequently, corrections for extinction based on the luminosity-weighted spectrum of the central region of a BCD can lead, in the case of Mrk 409, to a severe over-estimation of the H α luminosity and star formation rate.
- Mrk 409 shows a relatively high oxygen abundance ($12 + \log(\text{O}/\text{H}) \sim 8.40$), without evidence for any significant chemical abundance gradient out to $R \sim 0.6$ kpc.
- All the studied circumnuclear H II regions have electron densities in the low density limit. In the nuclear starburst region the electron density increases to a value as large as 500 cm^{-3} .
- The ionized gas component within the inner ~ 1 kpc of Mrk 409 displays a smooth kinematical pattern which is likely dominated by rotation; the total mass inside the SF ring is estimated to be $\simeq 1.4 \times 10^9 M_{\odot}$.

LMC and CK acknowledge the Alexander von Humboldt Foundation. NC and CZ are grateful for the hospitality of the Astrophysikalisches Institut Potsdam. We thank Begoña García-Lorenzo and Ana Monreal-Ibero for useful suggestions. We also thank José N.

González-Pérez, José M. Vílchez and Inma Martínez-Valpuesta for fruitful discussions. This research has made use of the NASA/IPAC Extragalactic Database (NED), which is operated by the Jet Propulsion Laboratory, Caltech, under contract with the National Aeronautics and Space Administration. The authors acknowledge the work of the Sloan Digital Sky Survey (SDSS) team. Funding for the SDSS has been provided by the Alfred P. Sloan Foundation, the Participating Institutions, the National Aeronautics and Space Administration, the National Science Foundation, the U.S. Department of Energy, the Japanese Monbukagakusho, and the Max Planck Society. The SDSS Web site is <http://www.sdss.org/>. This work has been partially funded by the Spanish “Ministerio de Ciencia e Innovación” through grants AYA 2007 67965 and HA2006-0032, and under the Consolider-Ingenio 2010 Program grant CSD2006-00070: First Science with the GTC (<http://www.iac.es/consolider-ingenio-gtc/>).

REFERENCES

- Alloin, D., Collin-Souffrin, S., Joly, M., & Vigroux, L. 1979, *A&A*, 78, 200
- Baldwin, J. A., Phillips, M. M., & Terlevich, R. 1981, *PASP*, 93, 5
- Brocklehurst, M. 1971, *MNRAS*, 153, 471
- Bruzual, G., & Charlot, S. 2003, *MNRAS*, 344, 1000
- Buta, R. 1988, *ApJS*, 66, 233
- Buta, R., & Crocker, D. A. 1993, *AJ*, 105, 1344
- Buta, R., & Purcell, G. B. 1998, *AJ*, 115, 484
- Cairós, L. M., Caon, N., Vílchez, J. M., González-Pérez, J. N., & Muñoz-Tuñón, C. 2001, *ApJS*, 136, 393
- Cairós, L. M., Caon, N., García-Lorenzo, B., Vílchez, J. M., & Muñoz-Tuñón, C. 2002, *ApJ*, 577, 164
- Cairós, L. M., Caon, N., García-Lorenzo, B., Monreal-Ibero, A., Amorín, R., Weilbacher, P., & Papaderos, P. 2007, *ApJ*, 669, 251
- Cairós, L. M., Caon, N., Zurita, C., Kehrig, C., Weilbacher, P., & Roth, M. 2009, *arXiv:0908.1305*
- Cid Fernandes, R., Gu, Q., Melnick, J., Terlevich, E., Terlevich, R., Kunth, D., Rodrigues Lacerda, R., & Joguet, B. 2004, *MNRAS*, 355, 273

- Cid Fernandes, R., González Delgado, R. M., Storchi-Bergmann, T., Martins, L. P., & Schmitt, H. 2005a, MNRAS, 356, 270
- Cid Fernandes, R., Mateus, A., Sodré, L., Stasińska, G., & Gomes, J. M. 2005b, MNRAS, 358, 363
- Combes, F., Gerin, M. 1985, A&A, 150, 327
- Comeron, S., Knapen, J. H., Beckman, J. E., Laurikainen, E., Salo, H., Martínez-Valpuesta, I., & Buta, R. J. 2009, MNRAS, in press
- Diaz, A. I., Terlevich, E., Castellanos, M., & Hägele, G. F. 2007, MNRAS, 382, 251
- Edmunds, M. G., & Pagel, B. E. J. 1984, MNRAS, 211, 507
- Fioc, M., & Rocca-Volmerange, B. 1997, A&A, 326, 950
- Fricke, K. J., Izotov, Y. I., Papaderos, P., Guseva, N. G., & Thuan, T. X. 2001, AJ, 121, 169
- García-Lorenzo, B., Cairós, L. M., Caon, N., Monreal-Ibero, A., & Kehrig, C. 2008, ApJ, 677, 201
- Garcia-Rissmann, A., Vega, L. R., Asari, N. V., Cid Fernandes, R., Schmitt, H., González Delgado, R. M., & Storchi-Bergmann, T. 2005, MNRAS, 359, 765
- Gil de Paz, A., Zamorano, J., Gallego, J., & Domínguez, F. 2000a, A&AS, 145, 377
- Gil de Paz, A., Zamorano, J., & Gallego, J. 2000b, A&A, 361, 465
- Gil de Paz, A., Silich, S. A., Madore, B. F., Sánchez Contreras, C., Zamorano, J., & Gallego, J. 2002, ApJ, 573, L101
- Gil de Paz, A., Madore, B. F., Noeske, K., Cairós, L. M., Papaderos, P., & Silich, S. A. 2003a, ApJ, 596, L179 (GdP03)
- Gil de Paz, A., Madore, B. F., & Pevunova, O. 2003b, ApJS, 147, 29
- Gil de Paz, A., & Madore, B. F. 2005, ApJS, 156, 345
- González Delgado, R. M., Heckman, T., & Leitherer, C. 2001, ApJ, 546, 845
- Guseva, N. G., Izotov, Y. I., Papaderos, P., Chaffee, F. H., Foltz, C. B., Green, R. F., Thuan, T. X., Fricke, K. J., Noeske, K. G. 2001, A&A, 378, 756

- Guseva, N. G., Papaderos, P., Izotov, Y. I., Green, R. F., Fricke, K. J., Thuan, T. X., & Noeske, K. G. 2003, *A&A*, 407, 105
- Izotov, Y. I., Schaerer, D., Blecha, A., Royer, F., Guseva, N. G., & North, P. 2006, *A&A*, 459, 71
- Izotov, Y. I., Thuan, T. X., & Stasińska, G. 2007, *ApJ*, 662, 15
- Izotov, Y. I., & Thuan, T. X. 2008, *ApJ*, 687, 133
- Johnson, K. E., Leitherer, C., Vacca, W. D., Conti, P. 2000, *AJ*, 120, 1273
- Kauffmann, G., White, S. D. M., & Guiderdoni, B. 1993, *MNRAS*, 264, 201
- Kehrig, C., Vílchez, J. M., Sánchez, S. F., Telles, E., Pérez-Montero, E., & Martín-Gordón, D. 2008, *A&A*, 477, 813
- Kelz, A., et al. 2006, *PASP*, 118, 129
- Kewley, L. J., & Ellison, S. L. 2008, *ApJ*, 681, 1183.
- Kewley, L. J., Dopita, M. A., Sutherland, R. S., Heisler, C. A., & Trevena, J. 2001, *ApJ*, 556, 121
- Kobulnicky, H. A., Kennicutt, R. C., Jr., & Pizagno, J. L. 1999, *ApJ*, 514, 544
- Kotilainen, J. K., Reunanen, J., Laine, S., & Ryder, S. D. 2000, *A&A*, 353, 834
- Krajnović, D., Cappellari, M., de Zeeuw, P. T., & Copin, Y. 2006, *MNRAS*, 366, 787
- Krüger, H., & Fritze-v. Alvensleben, U. 1994, *A&A*, 284, 793
- Lagos, P., Telles, E., Muñoz-Tuñón, C., Carrasco, E. R., Cuisinier, F., & Tenorio-Tagle, G. 2009, *AJ*, 137, 5068
- Legrand, F., Kunth, D., Mas-Hesse, J. M., & Lequeux, J. 1997, *A&A*, 326, 929
- Leitherer, C., et al. 1999, *ApJS*, 123, 3
- Lequeux, J. 1983, *A&A*, 125, 394
- Loose, H.-H., & Thuan, T. X. 1986, *Star-forming Dwarf Galaxies and Related Objects*, 73
- Markwardt, C. B. 2009, *Astronomical Society of the Pacific Conference Series*, 411, 251
- Mas-Hesse, J. M., & Kunth, D. 1999, *A&A*, 349, 765

- McCray, R., & Kafatos, M. 1987, ApJ, 317, 190
- McGaugh, S. S. 1991, ApJ, 380, 140
- Marlowe, A. T., Heckman, T. M., Wyse, R. F. G., & Schommer, R. 1995, ApJ, 438, 563
- Martin, C. L. 1997, ApJ, 491, 561
- Mas-Hesse, J. M., & Kunth, D. 1999, A&A, 349, 765
- Meurer, G. R., Freeman, K. C., Dopita, M. A., & Cacciari, C. 1992, AJ, 103, 60
- Miller, J. S., & Mathews, W. G. 1972, ApJ, 172, 593
- Noeske, K. G., Guseva, N. G., Fricke, K. J., Izotov, Y. I., Papaderos, P., & Thuan, T. X. 2000, A&A, 361, 33
- Osterbrock, D. E., & Ferland, G. J. 2006, *Astrophysics of gaseous nebulae and active galactic nuclei*, 2nd. ed. by D. E. Osterbrock and G. J. Ferland. Sausalito, CA: University Science Books, 2006
- Östlin, G., Zackrisson, E., Bergvall, N., & Ronnback, J. 2003, A&A, 408, 887
- Pagel, B. E. J., Edmunds, M. G., Blackwell, D. E., Chun, M. S., & Smith, G. 1979, MNRAS, 189, 95
- Pagel, B. E. J., Simonson, E. A., Terlevich, R. J., & Edmunds, M. G. 1992, MNRAS, 255, 325
- Papaderos, P., Loose, H.-H., Fricke, K. J., & Thuan, T. X. 1996b, A&A, 314, 59 (P96)
- Papaderos, P., Izotov, Y. I., Fricke, K. J., Thuan, T. X., & Guseva, N. G. 1998, A&A, 338, 43
- Papaderos, P., & Fricke, K. J. 1999, in *Highlights in X-ray Astronomy*, 193
- Papaderos, P., Izotov, Y. I., Thuan, T. X., Noeske, K. G., Fricke, K. J., Guseva, N. G., & Green, R. F. 2002, A&A, 393, 461
- Papaderos, P., Guseva, N. G., Izotov, Y. I., Noeske, K. G., Thuan, T. X., & Fricke, K. J. 2006, A&A, 457, 45
- Papaderos, P., Guseva, N. G., Izotov, Y. I., & Fricke, K. J. 2008, A&A, 491, 113
- Pérez-Montero, E., & Díaz, A. I. 2005, MNRAS, 361, 1063

- Pettini, M., & Pagel, B. E. J. 2004, MNRAS, 348, L59
- Pilyugin, L. S., Thuan, T. X., & Vílchez, J. M. 2006, MNRAS, 367, 1139
- De Robertis, M. M., Dufour, R. J., & Hunt, R. W. 1987, JRASC, 81, 195
- Roth, M. M., et al. 2005, PASP, 117, 620
- Sargent, W. L. W. & Searle, L. 1970, ApJ, 162, L155
- Schlegel, D. J., Finkbeiner, D. P., & Davis, M. 1998, ApJ, 500, 525
- Shaw, R. A., & Dufour, R. J. 1995, PASP, 107, 896
- Storchi-Bergmann, T., Schmitt, H. R., Calzetti, D., & Kinney, A. L. 1998, AJ, 115, 909
- Thuan, T. X. & Martin, G. E. 1981, ApJ, 247, 823
- Thuan, T. X., Izotov, Y. I., & Lipovetsky, V. A. 1997, ApJ, 477, 661
- Thuan, T. X., Izotov, Y. I., & Foltz, C. B. 1999, ApJ, 525, 105
- van Eymeren, J., Bomans, D. J., Weis, K., Dettmar, R.-J. 2007, A&A, 474, 67
- Veilleux, S., & Osterbrock, D. E. 1987, ApJS, 63, 295
- Vílchez, J. M., & Esteban, C. 1996, MNRAS, 280, 720
- Whitford, A. E. 1958, AJ, 63, 201
- Wilson, A. S., Baldwin, J. A., Sun, S.-D., & Wright, A. E. 1986, ApJ, 310, 121